ACS Partner Journal
PRECISION CHEMISTRY

pubs.acs.org/PrecisionChem
Article

Regulation of Coordinating Anions around Single Co(II) Sites in a Covalent Organic Framework for Boosting CO_2 Photoreduction

Nan Dai,[▽] Yunyang Qian,[▽] Denan Wang, Jiajia Huang, Xinyu Guan, Zhongyuan Lin, Weijie Yang, Rui Wang,* Jier Huang, Shuang-Quan Zang, and Hai-Long Jiang*

Cite This: *Precis. Chem.* 2024, 2, 600−609

ABSTRACT: While photocatalytic CO_2 reduction has been intensively investigated, reports on the influence of anions coordinated to catalytic metal sites on CO_2 photoreduction remain limited. Herein, different coordinated anions (F^-, Cl^-, OAc^-, and NO_3^-) around single Co sites installed on bipyridine-based three-component covalent organic frameworks (COFs) were synthesized, affording TBD-COF-Co-X (X = F, Cl, OAc, and NO_3), for photocatalytic CO_2 reduction. Notably, the presence of these coordinated anions on the Co sites significantly influences the photocatalytic performance, where TBD-COF-Co-F exhibits superior activity to its counterparts. Combined experimental and theoretical results indicate that the enhanced activity in TBD-COF-Co-F is attributed to its efficient charge transfer, high CO_2 adsorption capacity, and low energy barrier for CO_2 activation. This study provides a new strategy for boosting COF photocatalysis through coordinated anion regulation around catalytic metal sites.

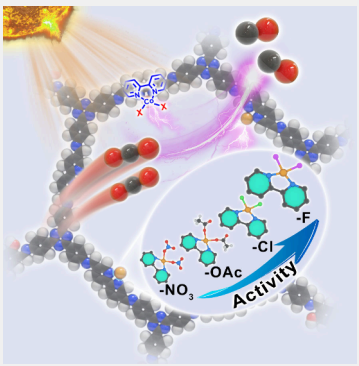

KEYWORDS: *covalent organic framework, single sites, CO_2 photoreduction, coordination environment, anion regulation*

INTRODUCTION

Escalating global warming and the energy crisis have raised alarm worldwide, underscoring the urgent need to control and reduce atmospheric CO_2 concentrations. Photocatalytic reduction of CO_2 has emerged as a promising strategy, offering an effective avenue for harnessing renewable energy and tackling the global issue of excessive carbon emissions.[1−3] However, the development of photocatalytic CO_2 reduction faces challenges such as inefficient photocatalysts, low CO_2 adsorption capacity, difficulties in CO_2 activation, etc. In light of these hurdles, the development of efficient photocatalysts for CO_2 reduction is urgently needed.

A wide array of photocatalysts have been developed to conduct photocatalytic CO_2 reduction, aiming for high conversion, improved selectivity, and high-value products.[4−8] Among these, single-site catalysts, featuring highly dispersed active metal sites, combine the benefits of both homogeneous and heterogeneous catalysts and have demonstrated great potential in photocatalytic CO_2 reduction.[9−11] With these findings, numerous strategies have been attempted to boost charge transfer in photocatalysts and/or to enhance the interaction between the catalytic site and CO_2, including altering the types of metal sites, adjusting the distance between the photosensitizer and the active site, and modifying the functional groups around the catalytic sites.[12−14] However, the influence of coordinated anions, a critical element of the catalytic metal sites, has seldom been investigated.[15] In addition, most of the single-atom catalysts prepared through pyrolysis tend to possess vague structures and limited tailorability.[16−19] Consequently, it is essential to construct a well-defined photocatalyst that includes catalytic metal sites with tunable coordination anions to thoroughly explore the influence of coordinated anions.

In this context, covalent organic frameworks (COFs), a class of porous crystalline materials composed of organic components linked by covalent bonds, have garnered considerable attention.[20−34] These materials exhibit extended conjugated structures that possess an excellent light absorption ability. Simultaneously, their customizable building blocks enable tailored structural design. Additionally, the pore spaces within COFs offer abundant opportunities for anchoring active metals, coupled with facilitated CO_2 enrichment and transportation.[35−42] More importantly, their organic skeletons endow them with the ability to precisely install metal sites and surrounding microenvironmental groups, making COFs very promising in the investigation of the structure−performance relationship toward CO_2 photoreduction.[43−49] Given these features, COFs are ideal platforms for studying the influence of coordinated anions around single metal sites on photocatalytic CO_2 reduction.

Received: July 9, 2024
Revised: September 22, 2024
Accepted: September 24, 2024
Published: October 14, 2024

https://doi.org/10.1021/prechem.4c00058
Precis. Chem. 2024, 2, 600−609

Herein, a novel bipyridine-based three-component TBD-COF is deliberately synthesized to install single Co(II) sites with different coordinating anions for the photocatalytic reduction of CO_2. The resulting four single-site Co(II) catalysts, namely, TBD-COF-Co-X (X = F, Cl, OAc, NO_3, where X represents the respective anions), feature the same COF skeleton with different coordinated anions around Co sites (Scheme 1). The resulting TBD-COF-Co-X exhibits

Scheme 1. Illustration Showing the Stepwise Synthesis of TBD-COF-Co-X (X = F, Cl, OAc, NO_3)

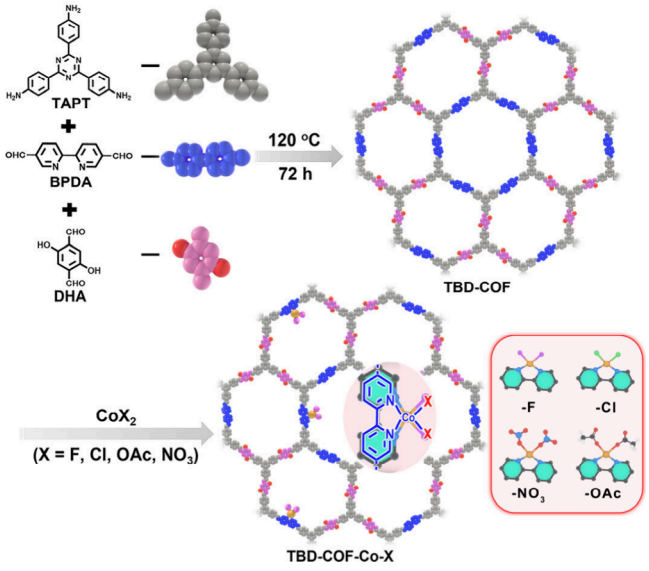

distinct CO production activity with altered coordinating anions in photocatalytic CO_2 reduction. Notably, TBD-COF-Co-F exhibits excellent performance, with a CO production rate of 504 $\mu mol \cdot g^{-1} \cdot h^{-1}$ and >98% selectivity to CO. Combined experimental and theoretical results reveal that the coordinating anions not only regulate the kinetics of charge transfer but also affect the electronic density of single Co(II) sites, resulting in different activation barriers for the key intermediates of CO_2 photoreduction. This study highlights the unique advantages of COFs as ideal platforms for designing and tailoring the coordination microenvironment of single metal sites in photocatalysis.

RESULTS AND DISCUSSION

The three-component TBD-COF was synthesized via Schiff base condensation between the aldehyde monomers of 2,5-dihydroxyterephthalaldehyde (DHA) and 2,2′-bipyridyl-5,5′-dialdehyde (BPDA) and the amine monomer of 1,3,5-tris(4-aminophenyl)triazine (TAPT) under solvothermal conditions. The DHA, serving as one of the mixed aldehyde monomers, ensures enhanced crystallinity and stability owing to the formation of a hydrogen bond (OH···N═C).[50] Concurrently, BPDA featuring a classical bipyridyl moiety is employed for subsequent metal incorporation. The ^1H nuclear magnetic resonance (NMR) spectra confirm a DHA-to-BPDA ratio of approximately 1:1 in TBD-COF (Figure 1a). The crystal structure of TBD-COF is verified through powder X-ray diffraction (XRD) analysis. The predicted powder XRD patterns, based on the DHA/BPDA ratio, strongly agree with the experimental results, corroborating the structure and AA stacking mode of the TBD-COF (Figure 1b, Figure S1, and Table S1). The solid-state ^{13}C CP-MAS NMR spectrum further validates the successful synthesis of TBD-COF (Figure S2). Fourier transform infrared (FT-IR) spectra are collected to determine the chemical information on the imine linkages (Figure 1c). In the FT-IR spectra, both the C═O stretching vibrations of DHA (1673 cm^{-1}) and BPDA (1684 cm^{-1}), as well as the N−H stretching vibration of TAPT (3323 cm^{-1}), are absent in TBD-COF and replaced by a new peak at 1620 cm^{-1} corresponding to the imine bond. The porosity and pore size distribution of TBD-COF are evaluated via N_2 sorption measurements at 77 K. The COF exhibited a Brunauer−Emmett−Teller (BET) surface area of approximately 1628 $m^2 \cdot g^{-1}$ (Figure S3), indicating the porous feature. Transmission electron microscopy (TEM) and scanning electron microscopy (SEM) observations reveal that TBD-COF possesses a lamellar stacked structure and a spherical morphology with an average diameter of ∼300 nm (Figures S4 and S5). Moreover, TBD-COF demonstrates significant visible light absorption attributed to its extended conjugated skeleton, indicating its potential as a visible-light photocatalyst (Figure 1d).

The single-site cobalt catalysts were successfully fabricated through the facile incorporation of Co salts (CoF_2/$CoCl_2$/$Co(OAc)_2$/$Co(NO_3)_2$) into the bipyridine moiety of TBD-COF, affording TBD-COF-Co-X (X = F, Cl, OAc, NO_3). This gives a consistent Co loading of approximately 1.0 wt % across all the samples, as confirmed by inductively coupled plasma atomic emission spectroscopy (ICP-AES) (Table S2). Powder XRD patterns and FT-IR spectra for all these samples were consistent with those of the pristine TBD-COF, indicating that the integration of Co(II) sites with various anions does not affect the skeleton and crystallinity (Figures S6 and S7). Additionally, nitrogen sorption isotherms demonstrate that the porous structure remains unchanged after the incorporation of different Co(II) complexes (Figure S8). The BET surface areas of TBD-COF-Co-X (X = F, Cl, OAc, NO_3) are 1276, 842, 1041, and 786 $m^2 \cdot g^{-1}$, respectively. The distinction is primarily due to the differences in the sizes of the coordinating anions and their crystallinity, as observed in the XRD patterns (Figure S6). Both SEM and TEM images suggest that the morphology of TBD-COF is maintained in TBD-COF-Co-F, and no visible Co nanoparticles can be detected (Figure S9).

X-ray photoelectron spectroscopy (XPS) is used to evaluate the electronic structures of the Co species in TBD-COF-Co-X (X = F, Cl, OAc, NO_3). The results indicate that the oxidation state of the Co species was +2 in all the samples,[51] and the order of the binding energies of Co $2p_{3/2}$ is TBD-COF-Co-F (781.5 eV) > TBD-COF-Co-Cl (781.4 eV) > TBD-COF-Co-OAc (781.3 eV) > TBD-COF-Co-NO_3 (781.2 eV) (Figure 2a), suggesting that the Co(II) electronic density follows the reversed sequence: TBD-COF-Co-F < TBD-COF-Co-Cl < TBD-COF-Co-OAc < TBD-COF-Co-NO_3. To further reveal the local coordination structure of the Co(II) center in TBD-COF-Co-X, X-ray absorption spectroscopy (XAS) was employed. The X-ray absorption near-edge structure (XANES) spectrum for the Co K-edge of TBD-COF-Co-F was shifted toward higher value of photoenergy compared to that of Co foil and showed a very similar edge position to the other two Co(II) samples, proving that the valence of Co is in +2 oxidation state (Figure 2b). Similarly, the same phenomenon can be observed for TBD-COF-Co-X (X = Cl, OAc, NO_3), which is in good agreement with the XPS analysis (Figures S10−S12). Furthermore, in the XANES spectra of the Co K-edge, the absorption edge energy increases in the order

https://doi.org/10.1021/prechem.4c00058
Precis. Chem. 2024, 2, 600−609

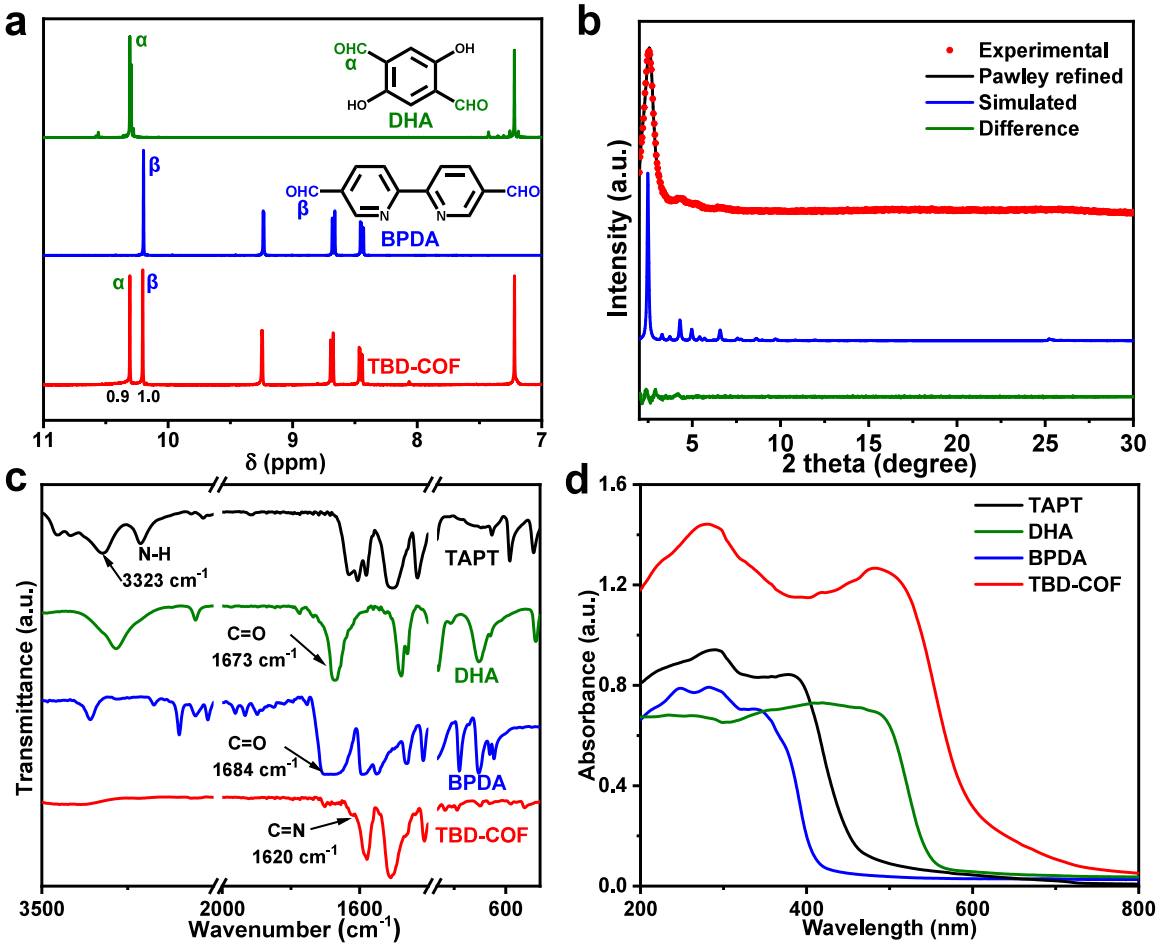

Figure 1. (a) ^{1}H NMR spectra of DHA, BPDA, and TBD-COF (α and β refer to the aldehyde hydrogen signals of DHA and BPDA, respectively). (b) Powder XRD pattern of TBD-COF. The green plot at the bottom shows the difference pattern between the experimental and Pawley refined data. (c) FT-IR and (d) UV−visible spectra of TBD-COF and its monomers.

of TBD-COF-Co-NO_3, TBD-COF-Co-OAc, TBD-COF-Co-Cl, and TBD-COF-Co-F, suggesting a gradual increase in the valence of Co from TBD-COF-Co-NO_3 to TBD-COF-Co-F (Figure S13). The Fourier transform-extended X-ray absorption fine structure (FT-EXAFS) spectrum of TBD-COF-Co-F exhibits a distinct peak at ∼1.54 Å, which can be attributed to Co−N;[52] moreover, the absence of any Co−Co bond-related peaks indicates that single Co(II) sites are preserved (Figure 2c). The EXAFS curve fitting is further adopted to confirm the coordination structure of the Co(II) sites in TBD-COF-Co-F. The bond distances of Co with the N atoms from bipyridine in TBD-COF-Co-F and bpy-Co-F (bpy refers to 4,4′-dimethyl-2,2′-bipyridine) are 2.09 and 2.08 Å, respectively, and the Co−F bond distance is 1.97 Å (Table S3). Therefore, the coordination configuration of TBD-COF-Co-F is determined, in which the Co atom is tetracoordinated with bipyridine and two F atoms (Figure 2d). In addition, the coordination structures of the Co sites in TBD-COF-Co-X (X = Cl, OAc, NO_3) based on the EXAFS data and theoretical structural models are also determined using a similar fitting process, and the specific fitting parameters are provided in the Supporting Information (Figures S10−S12 and Table S3). Therefore, the single Co(II) sites were successfully constructed in TBD-COF, which share identical coordination configurations with the exception of coordinated anions.

Encouraged by the above results, photocatalytic CO_2 reduction experiments were performed to investigate the effect of coordinated anions around the Co(II) sites. Remarkably, CO_2 can be efficiently converted to CO with minimal H_2 production (selectivity >98%) over TBD-COF-Co-X (X = F, Cl, OAc, NO_3) in the presence of 1,3-dimethyl-2-phenyl-2*H*-benzimidazole (BIH) as a sacrificial reagent under visible light irradiation. No liquid products are detected by ion chromatography. Notably, the photocatalytic activity is highly dependent on the type of anion coordinated to the Co sites, showcasing the order of TBD-COF-Co-F (504 μmol·g^{-1}·h^{-1}; turnover frequency (TOF) = 2.85 h^{-1}) > TBD-COF-Co-Cl (392 μmol·g^{-1}·h^{-1}; TOF = 2.15 h^{-1}) > TBD-COF-Co-OAc (327 μmol·g^{-1}·h^{-1}; TOF = 1.69 h^{-1}) > TBD-COF-Co-NO_3 (280 μmol·g^{-1}·h^{-1}; TOF = 1.68 h^{-1}) (Figure 3a, Table S4). Another common sacrificial agent, TEOA, has been tested for the photocatalytic reaction, and the results exhibit a similar trend (Figure S14). Control experiments show that TBD-COF produces negligible amounts of CO, highlighting the critical role of chelating Co(II) sites in CO_2 photoreduction. Similarly, CoF_2 alone displays no CO production without a COF, suggesting that the COF serves as a photosensitizer in addition to dispersing the single Co sites. Notably, the photocatalytic activity over the physical mixture of TBD-COF and CoF_2 is much lower than that of TBD-COF-Co-F, revealing that anchoring the Co site on the TBD-COF skeleton is favorable

https://doi.org/10.1021/prechem.4c00058
Precis. Chem. 2024, 2, 600−609

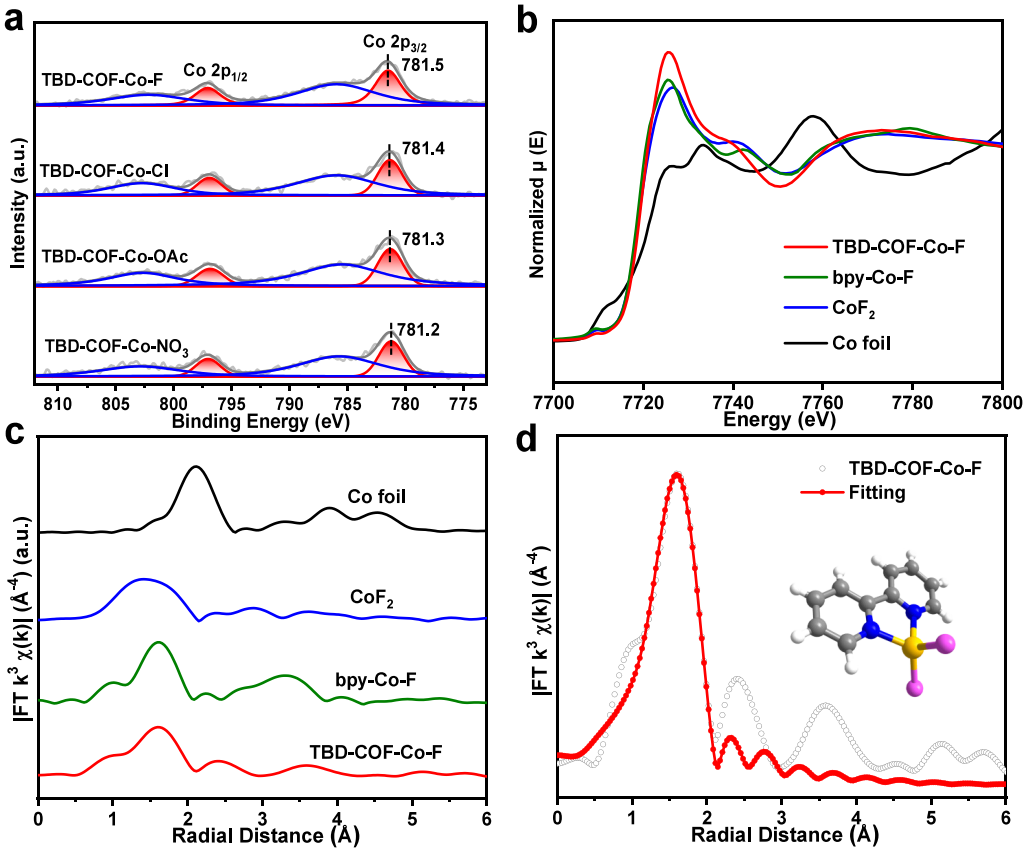

Figure 2. (a) The Co 2p XPS spectra of TBD-COF-Co-X (X = F, Cl, OAc, and NO_3). (b) Co K-edge XANES and (c) FT-EXAFS spectra of Co foil, CoF_2, bpy-Co-F and TBD-COF-Co-F. (d) EXAFS fitting of TBD-COF-Co-F (inset: proposed structure of the Co(II) sites in TBD-COF-Co-F (C, gray; H, white; N, blue; F, purple; and Co, orange).

for the transfer of photogenerated electrons. In addition, no products are detected in the absence of BIH or light or under a nitrogen atmosphere, underscoring the essential roles of the sacrificial agent, light irradiation, and CO_2 (Figure 3b). The stability of TBD-COF-Co-F is evaluated by recycling tests and corresponding characterization. The production rate and selectivity for the CO activity can be maintained for at least three cycles (Figure 3c). The crystallinity of the catalysts can be well maintained after the photocatalytic reaction according to the powder XRD patterns (Figure S15). TEM observation of TBD-COF-Co-F after the reaction indicates that no nanoparticles are formed, further demonstrating the stability of the catalyst (Figure S16). The Co content of TBD-COF-Co-F after the reaction is 0.979 wt %, similar to that of 1.043 wt % before the reaction, indicating that there is minimal metal leaching during the reaction. Furthermore, an isotopic experiment is conducted to determine the carbon source of CO. The ^{13}C-labeled CO_2 is introduced for photocatalytic CO_2 reduction, and the peak at m/z = 29 can be assigned to ^{13}CO, confirming that the CO product is generated from CO_2 rather than from other components in the catalytic system (Figure 3d).

To explain the difference in activity of TBD-COF-Co-X (X = F, Cl, OAc, NO_3), the mechanism of CO_2 photoreduction has been investigated. When excited at 380 nm, TBD-COF exhibits two prominent emission peaks at 425 and 505 nm. These emissions are notably quenched upon the gradual addition of a bpy-Co-F solution (Figure 4a). In contrast, the addition of bpy does not result in an evident quenching effect (Figure S17). This contrast suggests rapid electron transfer from the excited TBD-COF to the Co(II) site. Cyclic voltammetry (CV) tests were conducted on TBD-COF and TBD-COF-Co-F in Ar or a CO_2 atmosphere. TBD-COF exhibits neither a discernible redox potential nor a significant current variation under different atmospheres (Figure S18). In contrast, TBD-COF-Co-F displays a distinct reduction potential in an argon atmosphere: −1.07 V (vs NHE), which can be ascribed to the redox transitions of $Co^{II/I}$ (Figure 4b).[53,54] Notably, under a CO_2 atmosphere, the CV current of TBD-COF-Co-F exhibits a marked increase, suggesting enhanced electron transfer from TBD-COF-Co-F to CO_2, along with a new irreversible peak at −1.10 V (vs NHE) that can be ascribed to a $[Co\text{-}CO_2]^+$ adduct generated from the binding of Co^I and CO_2.[53,54] To comprehensively explore the reaction pathway for the photocatalytic CO_2 reduction, *in situ* diffuse reflectance infrared Fourier transform spectroscopy (DRIFTS) is employed to detect the reaction intermediates for TBD-COF-Co-F (Figure 4c). As the irradiation time is extended, the signals corresponding to the key intermediates of CO_2 reduction, namely, COOH* (1615 cm^{-1}) and CO* (2085 cm^{-1}), present gradual increases; furthermore, the signal at 1685 cm^{-1} can be attributed to bicarbonate formed through the interaction of H_2O and CO_2.[55] Consequently, in light of the aforementioned results, a mechanism for CO_2 photoreduction in TBD-COF-Co-X can be proposed (Figure S19).

Based on the above results, it is assumed that the difference in activity of TBD-COF-Co-X (X = F, Cl, OAc, NO_3) might be attributed to the following aspects: (1) light harvesting

https://doi.org/10.1021/prechem.4c00058
Precis. Chem. 2024, 2, 600−609

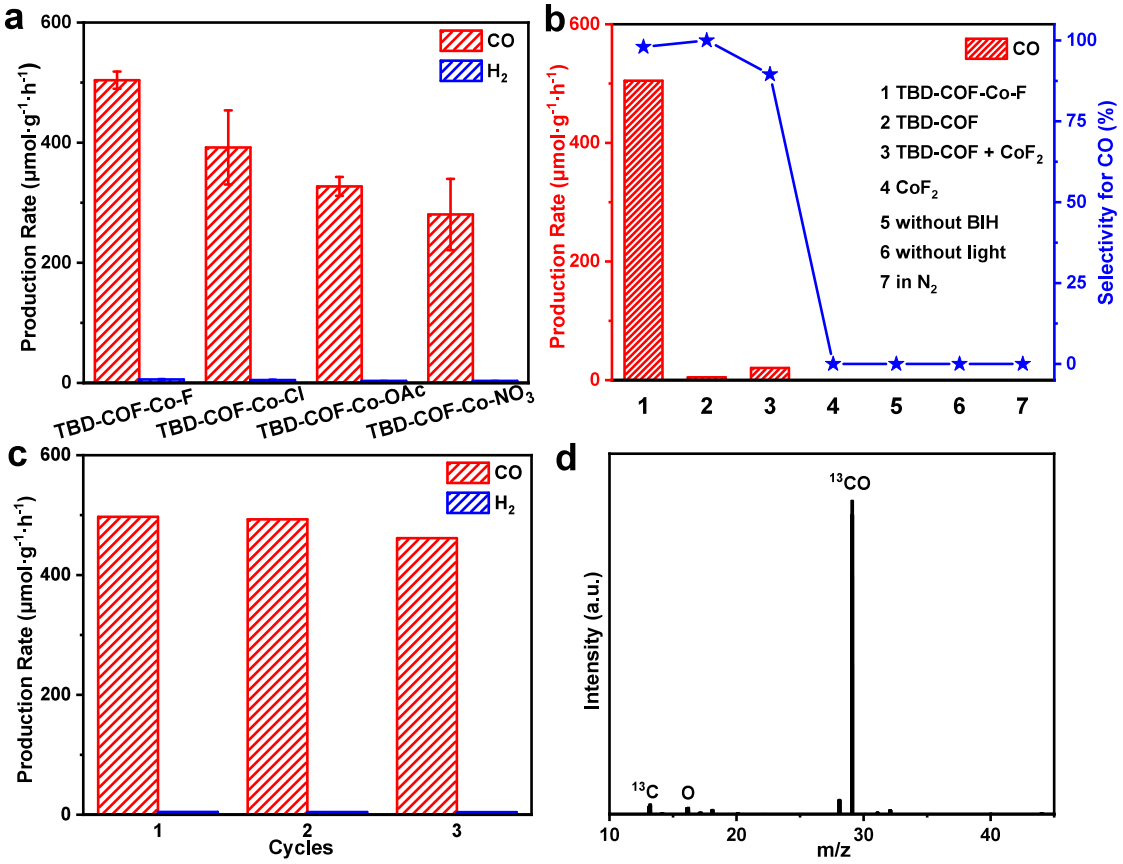

Figure 3. (a) Photocatalytic CO_2 reduction performance of TBD-COF-Co-X (X = F, Cl, OAc, and NO_3) (the error bars represent the relative deviation obtained from three parallel experiments). Reaction conditions: catalyst (5 mg), BIH (30 mg), CH_3CN (20 mL), $\lambda \geq 380$ nm, and CO_2 atmosphere. (b) Control experiments for photocatalytic CO_2 reduction. (c) Recycling performance of photocatalytic CO_2 reduction (2 h for each cycle). (d) GC-MS spectrum of ^{13}CO (m/z = 29) produced from the photocatalytic reduction of $^{13}CO_2$ over TBD-COF-Co-F.

ability, (2) charge transfer process, (3) CO_2 adsorption, and (4) CO_2 reduction process. First, the UV−vis spectra of TBD-COF-Co-X exhibit little variation, ruling out the effect of light absorption on photocatalytic activity (Figure S20). Furthermore, through combination with the Tauc plots and Mott−Schottky measurements, we can calculate the band structures of the four COFs (Figures S21−S24). The similar LUMO levels of the four COFs are more negative than the potential for CO_2 reduction to CO (−0.504 V vs NHE, pH 6.8),[56] indicating the feasibility of using these COFs for CO_2 photoreduction. Photoelectrochemical measurements were conducted to investigate the charge transfer process. According to the photoluminescence (PL) emission spectra, TBD-COF-Co-NO_3 displays the most pronounced emission peak, followed by TBD-COF-Co-OAc and TBD-COF-Co-Cl, while TBD-COF-Co-F exhibits the weakest intensity, indicating the most efficient charge separation in TBD-COF-Co-F (Figure S25). Moreover, compared with the other COFs, TBD-COF-Co-F demonstrates the strongest photocurrent response and has the smallest semicircle in the electrochemical impedance spectroscopy (EIS) Nyquist plots, suggesting a superior charge separation ability and minimum interfacial charge transfer resistance (Figures S26 and S27). Interestingly, the order of the other catalysts shows a similar tendency toward the CO_2 reduction activity. Therefore, the different coordinated anions of the single Co site are responsible for the charge transfer process in the photocatalysts. Subsequently, a CO_2 adsorption test is conducted to assess the CO_2 adsorption capacity. Notably, TBD-COF-Co-F exhibits an excellent CO_2 adsorption capacity at 298 K, surpassing the other three catalysts (Figure S28).

Furthermore, density functional theory (DFT) calculations have been conducted to compare the energy barriers of TBD-COF-Co-X (X = F, Cl, OAc, NO_3) during CO_2 reduction. The DRIFTS analysis reveals key intermediates, outlining the reaction paths of the CO_2RR to CO for subsequent calculations (Figure 4d and Figures S29−S31). The Gibbs free-energy calculations, coupled with the reaction paths of the CO_2RR, reveal that the rate-determining step for TBD-COF-Co-X (X = F, Cl, OAc, and NO_3) is the formation of the COOH* intermediate (Figure 4e and Table S5). Notably, the required free-energy change (ΔG) for COOH* in TBD-COF-Co-F is 0.655 eV, which is lower than those of TBD-COF-Co-Cl (0.702 eV), TBD-COF-Co-OAc (0.903 eV), and TBD-COF-Co-NO_3 (0.928 eV), aligning with the activity results. This suggests that the formation of COOH* (rate-determining step) is more likely at the Co sites in TBD-COF-Co-F. Consequently, the energy barrier for CO_2 activation can be controlled by coordinating anions, with TBD-COF-Co-F exhibiting the lowest energy barrier in the CO_2RR to CO. These findings unambiguously demonstrate that the coordinating anions effectively modulate the electronic structure of catalytic Co(II) sites, resulting in accelerated charge transfer kinetics, strong CO_2 adsorption, and a reduced energy barrier for enhanced performance in photocatalytic CO_2 reduction.

https://doi.org/10.1021/prechem.4c00058
Precis. Chem. 2024, 2, 600−609

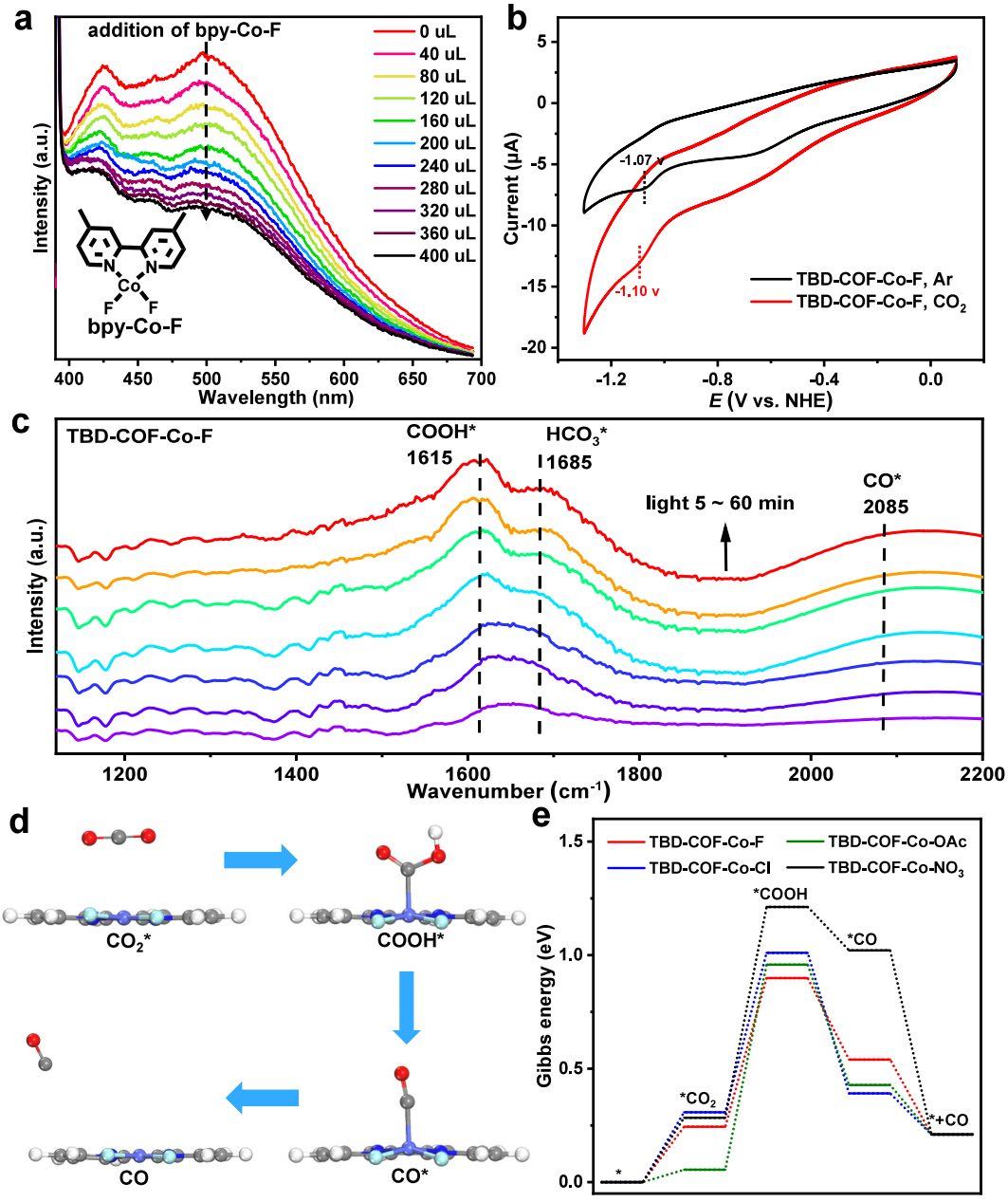

Figure 4. (a) Photoluminescence emission spectra (excited at 380 nm) of TBD-COF in CH_3CN upon the addition of bpy-Co-F. [TBD-COF] = 0.2 mg/mL, [bpy-Co-F] = 4 mg/mL. (b) Cyclic voltammetry results of TBD-COF-Co-F under CO_2 or Ar gas. Scan rate = 100 mV s^{-1}. (c) *In situ* DRIFTS spectra for the adsorption of the mixture of CO_2 and H_2O vapor on TBD-COF-Co-F under visible light irradiation >380 nm. (d) Structural models of the reaction path in photocatalytic CO_2 reduction by TBD-COF-Co-F (C, gray; H, white; O, red; N, blue; F, cyan; and Co, salvia blue). (e) Gibbs energy diagram of CO_2 reduction to CO over TBD-COF-Co-X (X = F, Cl, OAc, NO_3).

CONCLUSION

In summary, we have successfully fabricated single-site Co(II) catalysts with various coordinating anions based on the three-component COF as the support. The presence of distinct coordinated anions around the Co(II) sites in TBD-COF-Co-X (X = F, Cl, OAc, NO_3) is unequivocally confirmed through XAS analysis. Among them, TBD-COF-Co-F exhibits superior CO_2 photoreduction activity compared to the other three catalysts, highlighting the significant impact of coordination anions around the catalytic centers on catalysis. The variation in activity can be attributed to the differences in charge separation efficiency, CO_2 adsorption capacity, and energy barriers for CO_2 reduction to CO influenced by the coordinating anions. This work introduces a facile strategy for the precise modulation of coordinating anions around catalytic metal sites and, for the first time, demonstrates that the anions coordinating to the catalytic metal center can dominate the performance of COF-based photocatalytic systems.

EXPERIMENTAL SECTION

Materials and Instrumentation

All materials were purchased commercially and used directly unless otherwise stated. The 2,2′-bipyridyl-5,5′-dialdehyde was purchased from Jilin Extension Technology Ltd. The 2,5-dihydroxyterephtha-

https://doi.org/10.1021/prechem.4c00058
Precis. Chem. 2024, 2, 600−609

laldehyde and 2,4,6-tris(4-aminophenyl)-1,3,5-triazine were synthesized following previously reported methods.[57,58]

The ^{1}H NMR spectra were acquired using a Bruker AVANCE III NMR instrument (400 MHz). Solid NMR ^{13}C−CP/MAS spectra were recorded on a Bruker SB Avance III (500 MHz) spectrometer. Powder X-ray diffraction (PXRD) patterns were obtained using a Rigaku MiniFlex 600 X-ray diffractometer (Japan) operated at 45 kV and 200 mA with Cu Kα as the source (λ = 1.54178 Å). FT-IR spectroscopy was conducted in the 4000−400 wavenumber range on a Shimadzu IR Affinity-1 spectrometer. The Co content of the catalysts was determined with an Optima 7300 DV inductively coupled plasma atomic emission spectrometer. Nitrogen sorption at 77 K and CO_2 sorption at 298 K of the samples were tested using a Micromeritics ASAP 2020 physisorption instrument. The specific surface area was determined using the Brunauer−Emmett−Teller (BET) method, and the pore size distribution was calculated by employing the density functional theory (DFT) model. UV−vis diffuse reflectance spectra were obtained by using a Shimadzu UV-2700 spectrometer. Field emission scanning electron microscopy (FE-SEM) was conducted with a Zeiss Supra 40 scanning electron microscope at an accelerating voltage of 5 kV. XPS data were acquired by using an ESCALAB 250 high-performance electron spectrometer with monochromatic Al Kα ($h\nu$ = 1486.7 eV) as the excitation source. TEM images were obtained with a JEOL JEM-2100F field emission transmission electron microscope. Fluorescence emission spectra (excited at 380 nm) were measured by using a Hitachi FL-4600 fluorescence spectrometer. Gas-phase products from the photocatalytic experiments were analyzed by using a Shimadzu gas chromatograph (GC-2014). The XAS was conducted at beamline 12-BM at the Advanced Photon Source, Argonne National Laboratory.

Methods

Preparation of COFs. A long glass tube was filled with 20 mg of 2,4,6-tris(4-aminophenyl)-1,3,5-triazine, 11.9 mg of 2,2′-bipyridyl-5,5′-dialdehyde, and 4.7 mg of 2,5-dihydroxy-*p*-phenylenedicarboxaldehyde. Then, 0.9 mL of 1,3,5-trimethylbenzene and 0.1 mL of 1,4-dioxane were injected into the tube by syringe, and the mixture was sonicated for 10 min, followed by the addition of 40 μL of glacial acetic acid. The tube was flash frozen at 77 K (in a liquid N_2 bath), evacuated, and flame-sealed. The tubes were subsequently placed in an oven at 120 °C for 72 h to afford an orange-red precipitate. The solid was washed several times with THF until the supernatant was colorless and then washed twice with ethanol. The supernatant was removed, and the solid was dried under a vacuum at 60 °C.

Incorporation of Co sites in COFs. To synthesize the corresponding cobalt-based catalysts, 20 mg of the COF sample was placed in a glass vial. Subsequently, 7 mL of a solution containing a specific amount of cobalt salt was added. The cobalt salt solutions were prepared using different solvents: 36 μL of ethanol containing dissolved cobalt fluoride (10 mg/mL), 45 μL of acetonitrile containing dissolved cobalt chloride (10 mg/mL), 100 μL of ethanol containing dissolved cobalt acetate (10 mg/mL), or 110 μL of acetonitrile containing dissolved cobalt nitrate (10 mg/mL). These solutions were left at 25 °C for 24 h. After this step, the supernatant was removed, and the solid was washed with ethanol before being dried under a vacuum at 60 °C. The activated samples were then subjected to a vacuum at 120 °C.

Digestion of COFs. Typically, 3 mg of TBD-COF was dispersed in 2 mL of acetonitrile, followed by the addition of 200 μL of a 3 M HCl aqueous solution. The mixture was stirred overnight at 80 °C under a N_2 atmosphere. After the solution was cooled to room temperature, the pH of the solution was adjusted to 7 by adding saturated $NaHCO_3$ solution. The organic phase was extracted with chloroform, and the solvent was subsequently removed under a vacuum to afford the solid for ^{1}H NMR analysis.

XAS. The XAS spectra were acquired at beamline 12-BM at the Advanced Photon Source, Argonne National Laboratory. A fluorescence excitation mode was employed for all samples, and spectra were collected at room temperature by using a 13-element germanium solid-state detector. Reference spectra of the Co foil were obtained in transmission mode with ion chambers. The processing and analysis of the XAS data were conducted using Athena and Artemis software packages.

Electrochemical Measurements. Photocurrent tests were performed on a CHI 760e electrochemical workstation using a standard three-electrode system, with catalyst-covered FTO serving as the working electrode, a Pt electrode serving as the counter electrode, a saturated Ag/AgCl electrode serving as the reference electrode, and an electrolyte composed of a 0.1 M Na_2SO_4 solution. A 300 W xenon lamp (with a 380 nm filter) was used as the light source. To prepare the working electrode, 3 mg of solid sample was dispersed in 1 mL of ethanol, and 30 μL of Nafion solution was added. The mixture was sonicated for a few tens of seconds and then applied to the FTO electrode (1 cm × 1 cm), which was left to dry and used for photocurrent response testing, and the bias voltage was set to 0.9 V.

EIS and Mott−Schottky tests were performed on a Zahner Zennium electrochemical workstation using a standard three-electrode system with a Pt plate as the counter electrode, saturated Ag/AgCl as the reference electrode, and a 0.1 M Na_2SO_4 solution as the electrolyte. To prepare the working electrode, 3 mg of solid sample was dispersed in 500 μL of ethanol, and 10 μL of Nafion solution was added. Then, 30 μL of the mixture was added dropwise onto the glassy carbon electrode (Φ = 3 cm) in three times, and the electrode was subsequently left to dry for testing. The bias voltage was set to −1.6 V, and the Mott−Schottky frequencies were set to 500, 1000, and 2000 Hz.

Cyclic voltammetry tests were performed in a standard three-electrode system in a 10 mL cylindrical bottle with a Pt sheet as the counter electrode, Ag/AgCl as the reference electrode, a glassy carbon electrode precoated with catalyst TBD-COF-Co-F or TBD-COF as the working electrode, and an anhydrous acetonitrile solution containing 0.1 M tetrabutylammonium hexafluorophosphate as the electrolyte. Before each sweep of the CV curve, the bottle was continuously bubbled with Ar or CO_2 for 10 min.

Photocatalytic CO_2 Reduction. In a typical experiment, 5 mg of catalyst and 30 mg of BIH were dispersed in 20 mL of acetonitrile, and the mixture was sonicated for 2 min to obtain a uniform dispersion. The mixture was purged with CO_2 for 15 min. A 300 W xenon lamp with a filter ($\lambda \geq$ 380 nm) was used as the light source. After irradiation at 20 °C for 2 h, the products were quantified via gas chromatography (Shimadzu GC-2014, argon as a carrier gas) using a flame ionization detector (FID) and a thermal conductivity detector (TCD) to monitor the amount of CO and H_2.

For the recycling test, TBD-COF-Co-F was selected as the representative catalyst for stability testing in three rounds. The typical operation was the same as that in the above photocatalytic performance test, except that after each round of reaction the catalyst was separated by centrifugation to remove the supernatant and then used for the next round of reaction.

Fluorescence Quenching Experiments. Typically, 2 mg of TBD-COF was dispersed in 1 mL of acetonitrile and sonicated for 2 min. Then, 200 μL of the above mixture was diluted with 2.0 mL of acetonitrile. The excitation wavelength was set to 380 nm. The fluorescence intensity was recorded initially and again after each addition of 40 μL of an acetonitrile solution of bpy-Co-F or bpy (bpy = 4,4′-dimethyl-2,2′-bipyridine) for a total of 400 μL.

***In Situ* DRIFTS.** *In situ* DRIFTS measurements were conducted by using a Nicolet iST 10 spectrometer equipped with a mercury cadmium telluride detector. The catalyst powders were tightly compacted in a sample cell with a CaF_2 windows. To eliminate potential surface residues prior to testing, the sample was heated at 120 °C under an argon atmosphere for 30 min. After cooling to room temperature, a background spectrum was obtained under argon conditions. Subsequently, ultrapure CO_2 (99.999%), which was passed through a U-shaped tube containing water, was added to the system for 30 min. Next, the spectrum of the sample in the absence of light was recorded, and multiple spectra were subsequently acquired under continuous light irradiation ($\lambda \geq$ 380 nm) for up to 60 min. Notably, the final *in situ* DRIFTS spectra were collected by

https://doi.org/10.1021/prechem.4c00058
Precis. Chem. 2024, 2, 600−609

subtracting the spectrum recorded in the dark from the recorded spectra under light irradiation.

Theoretical Calculations. Based on DFT, structural optimizations and Gibbs energy calculations were applied via the Vienna ab initio simulation package (VASP).[59] The generalized gradient approximation (GGA) exchange-correlation functional was formulated with the Perdew–Burke–Ernzerhof (PBE) functional.[60] The projector augmented wave (PAW) potentials were performed to construct the pseudopotential.[61] All structures were fully relaxed with the convergence criteria for Hellmann–Feynman forces and the electronic self-consistency energy set to 0.02 eV $Å^{-1}$ and 10^{-6} eV, respectively. For all calculations, the plane-wave cutoff energy was 520 eV, and spin-polarization was applied with a single Γ-center *k*-point grid. To describe van der Waals interactions, a DFT-D3 method of Grimme with the Becke–Johnson damping function was employed.[62] Additionally, to adjust the strength of Coulomb and exchange interactions, the PBE+*U* method was carried out with U = 2.8 eV for Co 3d orbitals.[63] The Gibbs free energy changes (ΔG) of the CO_2RR were calculated from vibration frequency analysis.

■ ASSOCIATED CONTENT

Supporting Information

The Supporting Information is available free of charge at https://pubs.acs.org/doi/10.1021/prechem.4c00058.

Materials and instrumentation, material characterizations, and catalytic results (PDF)

■ AUTHOR INFORMATION

Corresponding Authors

Rui Wang − *College of Chemistry, Zhengzhou University, Zhengzhou, Henan 450001, China*; Email: wangruijy@zzu.edu.cn

Hai-Long Jiang − *Hefei National Research Center for Physical Sciences at the Microscale, Department of Chemistry, University of Science and Technology of China, Hefei, Anhui 230026, China*; orcid.org/0000-0002-2975-7977; Email: jianglab@ustc.edu.cn

Authors

Nan Dai − *Hefei National Research Center for Physical Sciences at the Microscale, Department of Chemistry, University of Science and Technology of China, Hefei, Anhui 230026, China; College of Chemistry, Zhengzhou University, Zhengzhou, Henan 450001, China; School of Chemistry and Pharmaceutical Engineering, Hefei Normal University, Hefei, Anhui 230061, China*

Yunyang Qian − *Hefei National Research Center for Physical Sciences at the Microscale, Department of Chemistry, University of Science and Technology of China, Hefei, Anhui 230026, China*; orcid.org/0000-0002-4802-1519

Denan Wang − *Department of Chemistry, Boston College, Chestnut Hill, Massachusetts 02467, United States*

Jiajia Huang − *Hefei National Research Center for Physical Sciences at the Microscale, Department of Chemistry, University of Science and Technology of China, Hefei, Anhui 230026, China*

Xinyu Guan − *Hefei National Research Center for Physical Sciences at the Microscale, Department of Chemistry, University of Science and Technology of China, Hefei, Anhui 230026, China*

Zhongyuan Lin − *Hefei National Research Center for Physical Sciences at the Microscale, Department of Chemistry, University of Science and Technology of China, Hefei, Anhui 230026, China*

Weijie Yang − *School of Energy and Power Engineering, North China Electric Power University, Baoding, Hebei 071003, China*; orcid.org/0000-0002-0232-1129

Jier Huang − *Department of Chemistry, Boston College, Chestnut Hill, Massachusetts 02467, United States*; orcid.org/0000-0002-2885-5786

Shuang-Quan Zang − *College of Chemistry, Zhengzhou University, Zhengzhou, Henan 450001, China*; orcid.org/0000-0002-6728-0559

Complete contact information is available at: https://pubs.acs.org/10.1021/prechem.4c00058

Author Contributions

[▽]N.D. and Y.Q. contributed equally to this work. The manuscript was written through the contributions of all authors. All authors have given approval for the final version of the manuscript.

Notes

The authors declare no competing financial interest.

■ ACKNOWLEDGMENTS

This work is supported by the National Key Research and Development Program of China (2021YFA1500400), the NSFC (U22A20401, 22331009, and 22205208), the Strategic Priority Research Program of the Chinese Academy of Sciences (XDB0450302 and XDB0540000), the Fundamental Research Funds for the Central Universities (WK9990000137), the Postdoctoral Fellowship Program of CPSF (GZC20232538 and GZC20232532), the China Postdoctoral Science Foundation (2024M753086), and Hefei Normal University 2023 Scientific Research Fund Project for Introducing High level Talents (2023rcjj11). The calculations in this work are supported by the Supercomputing Center of University of Science and Technology of China (USTC) and Hefei Advanced Computing Center. This work was partially carried out at the Instruments Center for Physical Science, USTC.

■ REFERENCES

(1) Chang, X.; Wang, T.; Gong, J. CO_2 photo-reduction: insights into CO_2 activation and reaction on surfaces of photocatalysts. *Energy Environ. Sci.* **2016**, *9*, 2177.

(2) Lin, W.; Lin, J.; Zhang, X.; Zhang, L.; Borse, R. A.; Wang, Y. Decoupled Artificial Photosynthesis via a Catalysis-Redox Coupled COF||$BiVO_4$ Photoelectrochemical Device. *J. Am. Chem. Soc.* **2023**, *145*, 18141.

(3) Li, X.; Yu, J.; Jaroniec, M.; Chen, X. Cocatalysts for Selective Photoreduction of CO_2 into Solar Fuels. *Chem. Rev.* **2019**, *119*, 3962.

(4) Kumagai, H.; Tamaki, Y.; Ishitani, O. Photocatalytic Systems for CO_2 Reduction: Metal-Complex Photocatalysts and Their Hybrids with Photofunctional Solid Materials. *Acc. Chem. Res.* **2022**, *55*, 978.

(5) Feng, C.; Bo, T.; Maity, P.; Zuo, S.; Zhou, W.; Huang, K.-W.; Mohammed, O. F.; Zhang, H. Regulating Photocatalytic CO_2 Reduction Kinetics through Modification of Surface Coordination Sphere. *Adv. Funct. Mater.* **2024**, *34*, No. 2309761.

(6) Wu, H.-L.; Li, X.-B; Tung, C.-H.; Wu, L.-Z. Semiconductor Quantum Dots: An Emerging Candidate for CO_2 Photoreduction. *Adv. Mater.* **2019**, *31*, No. 1900709.

(7) Gao, W.; Li, S.; He, H.; Li, X.; Cheng, Z.; Yang, Y.; Wang, J.; Shen, Q.; Wang, X.; Xiong, Y.; Zhou, Y.; Zou, Z. Vacancy-defect modulated pathway of photoreduction of CO_2 on single atomically thin $AgInP_2S_6$ sheets into olefiant gas. *Nat. Commun.* **2021**, *12*, 4747.

(8) Zhang, X.; Huang, W.; Yu, L.; García-Melchor, M.; Wang, D.; Zhi, L.; Zhang, H. Enabling heterogeneous catalysis to achieve carbon

neutrality: Directional catalytic conversion of CO_2 into carboxylic acids. *Carbon Energy* **2024**, *6*, No. e362.
(9) Huang, P.; Huang, J.; Pantovich, S. A.; Carl, A. D.; Fenton, T. G.; Caputo, C. A.; Grimm, R. L.; Frenkel, A. I.; Li, G. Selective CO_2 Reduction Catalyzed by Single Cobalt Sites on Carbon Nitride under Visible-Light Irradiation. *J. Am. Chem. Soc.* **2018**, *140*, 16042.
(10) Hasija, V.; Patial, S.; Raizada, P.; Khan, A. A. P.; Asiri, A. M.; Le, Q. V.; Nguyen, V. H.; Singh, P. Covalent organic frameworks promoted single metal atom catalysis: Strategies and applications. *Coord. Chem. Rev.* **2022**, *452*, No. 214298.
(11) Ma, B.; Chen, G.; Fave, C.; Chen, L.; Kuriki, R.; Maeda, K.; Ishitani, O.; Lau, T.-C.; Bonin, J.; Robert, M. Efficient Visible-Light-Driven CO_2 Reduction by a Cobalt Molecular Catalyst Covalently Linked to Mesoporous Carbon Nitride. *J. Am. Chem. Soc.* **2020**, *142*, 6188.
(12) Wang, G.; Chen, Z.; Wang, T.; Wang, D.; Mao, J. P and Cu Dual Sites on Graphitic Carbon Nitride for Photocatalytic CO_2 Reduction to Hydrocarbon Fuels with High C_2H_6 Evolution. *Angew. Chem., Int. Ed.* **2022**, *61*, No. e202210789.
(13) Li, J.; Huang, H.; Xue, W.; Sun, K.; Song, X.; Wu, C.; Nie, L.; Li, Y.; Liu, C.; Pan, Y.; Jiang, H.-L.; Mei, D.; Zhong, C. Self-adaptive dual-metal-site pairs in metal-organic frameworks for selective CO_2 photoreduction to CH_4. *Nat. Catal.* **2021**, *4*, 719.
(14) Feng, X.; Pi, Y.; Song, Y.; Brzezinski, C.; Xu, Z.; Li, Z.; Lin, W. Metal-Organic Frameworks Significantly Enhance Photocatalytic Hydrogen Evolution and CO_2 Reduction with Earth-Abundant Copper Photosensitizers. *J. Am. Chem. Soc.* **2020**, *142*, 690.
(15) Zhuo, T.-C.; Song, Y.; Zhuang, G.-L.; Chang, L.-P.; Yao, S.; Zhang, W.; Wang, Y.; Wang, P.; Lin, W.; Lu, T.-B.; Zhang, Z.-M. H-Bond-Mediated Selectivity Control of Formate versus CO during CO_2 Photoreduction with Two Cooperative Cu/X Sites. *J. Am. Chem. Soc.* **2021**, *143*, 6114.
(16) Zhao, C.-X.; Zhang, Q. Crafting Pyrolysis-Free M-N-C Catalysts. *Precis. Chem.* **2023**, *1*, 264.
(17) Gong, Y.-N.; Jiao, L.; Qian, Y.; Pan, C.-Y.; Zheng, L.; Cai, X.; Liu, B.; Yu, S.-H.; Jiang, H.-L. Regulating Coordination Environment of Single-Atom Ni Electrocatalysts Templated by MOF for Boosting CO_2 Reduction. *Angew. Chem., Int. Ed.* **2020**, *59*, 2705.
(18) Chang, B.; Zhang, H.; Sun, S.; Zhang, G. Strategies to achieve effective nitrogen activation. *Carbon Energy* **2024**, *6*, No. e491.
(19) Huang, W.; Bo, T.; Zuo, S.; Wang, Y.; Chen, J.; Ould-Chikh, S.; Li, Y.; Zhou, W.; Zhang, J.; Zhang, H. Surface decorated Ni sites for superior photocatalytic hydrogen production. *SusMater.* **2022**, *2*, 466.
(20) Diercks, C. S.; Yaghi, O. M. The atom, the molecule, and the covalent organic framework. *Science* **2017**, *355*, No. eaal1585.
(21) Wang, H.; Wang, H.; Wang, Z.; Tang, L.; Zeng, G.; Xu, P.; Chen, M.; Xiong, T.; Zhou, C.; Li, X.; Huang, D.; Zhu, Y.; Wang, Z.; Tang, J. Covalent organic framework photocatalysts: structures and applications. *Chem. Soc. Rev.* **2020**, *49*, 4135.
(22) Guan, Q.; Zhou, L.-L.; Dong, Y.-B. Metalated covalent organic frameworks: from synthetic strategies to diverse applications. *Chem. Soc. Rev.* **2022**, *51*, 6307.
(23) Gong, Y.-N.; Guan, X.; Jiang, H.-L. Covalent Organic Frameworks for Photocatalysis: Synthesis, Structural Features, Fundamentals and Performance. *Coord. Chem. Rev.* **2023**, *475*, No. 214889.
(24) Dong, J.; Han, X.; Liu, Y.; Li, H.; Cui, Y. Metal-Covalent Organic Frameworks (MCOFs): A Bridge Between Metal Organic Frameworks and Covalent Organic Frameworks. *Angew. Chem., Int. Ed.* **2020**, *59*, 13722.
(25) Zhu, Y.; Yan, Y.; Feng, Y.; Liu, Y.; Lin, C.-Y.; Ai, Q.; Zhai, T.; Shin, B.; Xu, R.; Shen, H.; Fang, Q.; Zhang, X.; Bhagwandin, D.; Han, Y.; Zhu, H.; Glavin, N. R.; Ajayan, P. M; Li, Q.; Lou, J. A General Synthesis Method for Covalent Organic Framework and Inorganic 2D Materials Hybrids. *Precision Chemistry* **2024**, *2*, 398−405.
(26) Yusran, Y.; Li, H.; Guan, X.; Fang, Q.; Qiu, S. Covalent Organic Frameworks for Catalysis. *Energychem* **2020**, *2*, No. 100035.
(27) Geng, K.; He, T.; Liu, R.; Dalapati, S.; Tan, K.; Li, Z.; Tao, S.; Gong, Y.; Jiang, Q.; Jiang, D. Covalent Organic Frameworks: Design, Synthesis, and Functions. *Chem. Rev.* **2020**, *120*, 8814.
(28) Wang, S.; Wu, T.; Wu, S.; Guo, J.; He, T.; Wu, Y.; Yuan, W.; Zhang, Z.; Hua, Y.; Zhao, Y. Cobaloxime-Integrated Covalent Organic Frameworks for Photocatalytic Hydrogen Evolution Coupled with Alcohol Oxidation. *Angew. Chem., Int. Ed.* **2023**, *62*, No. e202311082.
(29) Kang, C.; Zhang, Z.; Kusaka, S.; Negita, K.; Usadi, A. K.; Calabro, D. C.; Baugh, L. S.; Wang, Y.; Zou, X.; Huang, Z.; Matsuda, R.; Zhao, D. Covalent organic framework atropisomers with multiple gas-triggered structural flexibilities. *Nat. Mater.* **2023**, *22*, 636−643.
(30) Zhou, Z.-B.; Han, X.-H.; Qi, Q.-Y.; Gan, S.-X.; Ma, D.-L.; Zhao, X. A Facile, Efficient, and General Synthetic Method to Amide-Linked Covalent Organic Frameworks. *J. Am. Chem. Soc.* **2022**, *144*, 1138.
(31) Grunenberg, L.; Savasci, G.; Terban, M. W.; Duppel, V.; Moudrakovski, I.; Etter, M.; Dinnebier, R. E.; Ochsenfeld, C.; Lotsch, B. V. Amine-Linked Covalent Organic Frameworks as a Platform for Postsynthetic Structure Interconversion and Pore-Wall Modification. *J. Am. Chem. Soc.* **2021**, *143*, 3430.
(32) Zhao, X.; Pachfule, P.; Thomas, A. Covalent organic frameworks (COFs) for electrochemical applications. *Chem. Soc. Rev.* **2021**, *50*, 6871.
(33) Alsudairy, Z.; Brown, N.; Yang, C.; Cai, S.; Akram, F.; Ambus, A.; Ingram, C.; Li, X. Facile Microwave-Assisted Synthesis of 2D Imine-Linked Covalent Organic Frameworks for Exceptional Iodine Capture. *Precis. Chem.* **2023**, *1*, 233.
(34) Zhang, J.; Cheng, C.; Guan, L.; Jiang, H.-L.; Jin, S. Rapid Synthesis of Covalent Organic Frameworks with a Controlled Morphology: An Emulsion Polymerization Approach via the Phase Transfer Catalysis Mechanism. *J. Am. Chem. Soc.* **2023**, *145*, 21974.
(35) Yang, S.; Hu, W.; Zhang, X.; He, P.; Pattengale, B.; Liu, C.; Cendejas, M.; Hermans, I.; Zhang, X.; Zhang, J.; Huang, J. 2D covalent organic frameworks as intrinsic photocatalysts for visible light-driven CO_2 reduction. *J. Am. Chem. Soc.* **2018**, *140*, 14614.
(36) Lu, M.; Zhang, M.; Liu, J.; Chen, Y.; Liao, J.-P.; Yang, M.-Y.; Cai, Y.-P.; Li, S.-L.; Lan, Y.-Q. Covalent Organic Framework Based Functional Materials: Important Catalysts for Efficient CO_2 Utilization. *Angew. Chem., Int. Ed.* **2022**, *61*, No. e202200003.
(37) Zhang, M.; Liao, J.-P.; Li, R.-H.; Sun, S.-N.; Lu, M.; Dong, L.-Z.; Huang, P.; Li, S.-L.; Cai, Y.-P.; Lan, Y.-Q.Green Synthesis of Bifunctional Phthalocyanine-Porphyrin COFs in Water for Efficient Electrocatalytic CO2 Reduction Coupled with Methanol Oxidation. *Natl. Sci. Rev.* **2023**, *10*, DOI: 10.1093/nsr/nwad226.
(38) Lu, M.; Zhang, S.-B.; Yang, M.-Y.; Liu, Y.-F.; Liao, J.-P.; Huang, P.; Zhang, M.; Li, S.-L.; Su, Z.-M.; Lan, Y.-Q. Dual Photosensitizer Coupled Three-Dimensional Metal-Covalent Organic Frameworks for Efficient Photocatalytic Reactions. *Angew. Chem., Int. Ed.* **2023**, *62*, No. e202307632.
(39) Fu, Z.; Wang, X.; Gardner, A. M.; Wang, X.; Chong, S. Y.; Neri, G.; Cowan, A. J.; Liu, L.; Li, X.; Vogel, A.; Clowes, R.; Bilton, M.; Chen, L.; Sprick, R. S.; Cooper, A. I. A stable covalent organic framework for photocatalytic carbon dioxide reduction. *Chem. Sci.* **2020**, *11*, 543.
(40) Zhang, Q.; Gao, S.; Guo, Y.; Wang, H.; Wei, J.; Su, X.; Zhang, H.; Liu, Z.; Wang, J. Designing covalent organic frameworks with $Co-O_4$ atomic sites for efficient CO_2 photoreduction. *Nat. Commun.* **2023**, *14*, 1147.
(41) Cheng, Y.-Z.; Ji, W.; Hao, P.-Y.; Qi, X.-H.; Wu, X.; Dou, X.-M.; Bian, X.-Y.; Jiang, D.; Li, F.-T.; Liu, X.-F.; Yang, D.-H.; Ding, X.; Han, B.-H. A Fully Conjugated Covalent Organic Framework with Oxidative and Reductive Sites for Photocatalytic Carbon Dioxide Reduction with Water. *Angew. Chem., Int. Ed.* **2023**, *62*, No. e202308523.
(42) Wang, X.; Ding, X.; Jin, Y.; Qi, D.; Wang, H.; Han, Y.; Wang, T.; Jiang, J. Post-Nickelation of a Crystalline Trinuclear Copper Organic Framework for Synergistic Photocatalytic Carbon Dioxide Conversion. *Angew. Chem., Int. Ed.* **2023**, *62*, No. e202302808.

(43) Ran, L.; Li, Z.-W.; Ran, B.; Cao, J.-Q.; Zhao, Y.; Shao, T.; Song, Y.-R.; Leung, M. K. H.; Sun, L.-C.; Hou, J.-G. Engineering Single-Atom Active Sites on Covalent Organic Frameworks for Boosting CO_2 Photoreduction. *J. Am. Chem. Soc.* **2022**, *144*, 17097.
(44) Zhou, M.; Wang, Z.; Mei, A.; Yang, Z.; Chen, W.; Ou, S.; Wang, S.; Chen, K.; Reiss, P.; Qi, K.; Ma, J.; Liu, Y. Photocatalytic CO_2 reduction using La-Ni bimetallic sites within a covalent organic framework. *Nat. Commun.* **2023**, *14*, 2473.
(45) Mohata, S.; Das, R.; Koner, K.; Riyaz, M.; Das, K.; Chakraborty, S.; Ogaeri, Y.; Nishiyama, Y.; Peter, S. C.; Banerjee, R. Selective Metal-Free CO_2 Photoreduction in Water Using Porous Nanostructures with Internal Molecular Free Volume. *J. Am. Chem. Soc.* **2023**, *145*, 23802.
(46) Wang, X.; Fu, Z.; Zheng, L.; Zhao, C.; Wang, X.; Chong, S. Y.; McBride, F.; Raval, R.; Bilton, M.; Liu, L.; Wu, X.; Chen, L.; Sprick, R. S.; Cooper, A. I. Covalent Organic Framework Nanosheets Embedding Single Cobalt Sites for Photocatalytic Reduction of Carbon Dioxide. *Chem. Mater.* **2020**, *32*, 9107.
(47) Zhong, W.; Sa, R.; Li, L.; He, Y.; Li, L.; Bi, J.; Zhuang, Z.; Yu, Y.; Zou, Z. A Covalent Organic Framework Bearing Single Ni Sites as a Synergistic Photocatalyst for Selective Photoreduction of CO_2 to CO. *J. Am. Chem. Soc.* **2019**, *141*, 7615.
(48) Zhong, H.; Sa, R.; Lv, H.; Yang, S.; Yuan, D.; Wang, X.; Wang, R. Covalent Organic Framework Hosting Metalloporphyrin-Based Carbon Dots for Visible-Light-Driven Selective CO_2 Reduction. *Adv. Funct. Mater.* **2020**, *30*, No. 2002654.
(49) Ding, J.; Guan, X.; Lv, J.; Chen, X.; Zhang, Y.; Li, H.; Zhang, D.; Qiu, S.; Jiang, H.-L.; Fang, Q. Three-Dimensional Covalent Organic Frameworks with Ultra-Large Pores for Highly Efficient Photocatalysis. *J. Am. Chem. Soc.* **2023**, *145*, 3248.
(50) Kandambeth, S.; Shinde, D. B.; Panda, M. K.; Lukose, B.; Heine, T.; Banerjee, R. Enhancement of chemical stability and crystallinity in porphyrin-containing covalent organic frameworks by intramolecular hydrogen bonds. *Angew. Chem., Int. Ed.* **2013**, *52*, 13052.
(51) Gong, Y.-N.; Zhong, W.; Li, Y.; Qiu, Y.; Zheng, L.; Jiang, J.; Jiang, H.-L. Regulating Photocatalysis by Spin-State Manipulation of Cobalt in Covalent Organic Frameworks. *J. Am. Chem. Soc.* **2020**, *142*, 16723.
(52) Yang, S.; Pattengale, B.; Lee, S.; Huang, J. Real-Time Visualization of Active Species in a Single-Site Metal-Organic Framework Photocatalyst. *ACS Energy Lett.* **2018**, *3*, 532.
(53) Wang, J.-W.; Qiao, L.-Z.; Nie, H.-D.; Huang, H.-H.; Li, Y.; Yao, S.; Liu, M.; Zhang, Z.-M.; Kang, Z.-H.; Lu, T.-B. Facile electron delivery from graphene template to ultrathin metal-organic layers for boosting CO_2 photoreduction. *Nat. Commun.* **2021**, *12*, 813.
(54) Wang, J.-W.; Huang, H.-H.; Sun, J.-K.; Ouyang, T.; Zhong, D.-C.; Lu, T.-B. Electrocatalytic and Photocatalytic Reduction of CO_2 to CO by Cobalt(II) Tripodal Complexes: Low Overpotentials, High Efficiency and Selectivity. *ChemSusChem* **2018**, *11*, 1025.
(55) Li, X.; Sun, Y.; Xu, J.; Shao, Y.; Wu, J.; Xu, X.; Pan, Y.; Ju, H.; Zhu, J.; Xie, Y. Selective visible-light-driven photocatalytic CO_2 reduction to CH_4 mediated by atomically thin $CuIn_5S_8$ layers. *Nat. Energy* **2019**, *4*, 690.
(56) Sun, K.; Qian, Y.; Jiang, H.-L. Metal-Organic Frameworks for Photocatalytic Water Splitting and CO_2 Reduction. *Angew. Chem., Int. Ed.* **2023**, *62*, No. e202217565.
(57) Jeon, S.; Park, S.; Nam, J.; Kang, Y.; Kim, J. Creating Patterned Conjugated Polymer Images Using Water-Compatible Reactive Inkjet Printing. *ACS Appl. Mater. Interfaces* **2016**, *8*, 1813.
(58) Bhanja, P.; Chatterjee, S.; Bhaumik, A. Triazine-Based Porous Organic Polymer with Good CO_2 Gas Adsorption Properties and an Efficient Organocatalyst for the One-Pot Multicomponent Condensation Reaction. *ChemCatChem.* **2016**, *8*, 3089.
(59) Kresse, G.; Furthmüller, J. Efficiency of ab initio total energy calculations for metals and semiconductors using a plane-wave basis set. *Comput. Mater. Sci.* **1996**, *6*, 15.
(60) Kresse, G.; Joubert, D. From ultrasoft pseudopotentials to the projector augmented-wave method. *Phys. Rev. B* **1999**, *59*, 1758.
(61) Blöchl, P. E. Projector augmented-wave method. *Phys. Rev. B* **1994**, *50*, 17953.
(62) Grimme, S.; Ehrlich, S.; Goerigk, L. Effect of the damping function in dispersion corrected density functional theory. *Comput. Chem.* **2011**, *32*, 1456.
(63) Peng, Y.-M.; Hajiyani, H.; Pentcheva, R. Influence of Fe and Ni Doping on the OER Performance at the Co_3O_4(001) Surface: Insights from DFT+U Calculations. *ACS Catal.* **2021**, *11*, 5601.

https://doi.org/10.1021/prechem.4c00058
Precis. Chem. 2024, 2, 600−609